Quantitative phase-field modeling of solidification in binary alloys with nonlinear phase coexistence curves

Chaohui Tong, Michael Greenwood, and Nikolas Provatas*
Department of Materials Science and Engineering and Brockhouse Institute for Materials Research, McMaster University, 1280 Main Street West, Ontario, Canada L8S-4 L7
(Received 29 June 2007; published 25 February 2008)

A formalism is presented for performing quantitative phase-field simulations of single-phase solidification in binary alloys with nonlinear solidus and liquidus curves. It is shown that, close to equilibrium, Gibbs free energy of an alloy phase can be approximated by the free energy function of a dilute ideal binary alloy, modified by *effective* temperature-dependent coefficients. This makes it possible to exploit a recent phase-field technique [A. Karma, Phys. Rev. Lett. **87**, 115701 (2001)] to model the free-boundary kinetics of single-phase solidification in binary alloys having nonlinear phase coexistence curves. Simulations of isothermal and nonisothermal dendritic solidification in an isomorphous binary alloy are used to demonstrate convergence of tip speed and radius for different values of the phase-field interface thickness. The effect linear versus nonlinear phase boundaries on dendritic tip speed is examined.

DOI: 10.1103/PhysRevB.77.064112 PACS number(s): 64.70.D−, 68.70.+w

I. INTRODUCTION

The study of microstructural evolution in solidification is at the heart of many problems of scientific and engineering significance. In recent years, the phase-field method has emerged as a powerful tool to tackle such free-boundary problems. This method has the advantage that it avoids explicit front tracking by making phase boundaries spatially diffuse through the use of order parameters that vary continuously across interfaces. However, the multiscale nature of solidification makes it difficult to use phase-field models *quantitatively* because of the computational complexity associated with making the solid-liquid interface thin enough to mimic the desired sharp-interface limit.

The computational complexity that arises when setting the phase-field interface width (W) to realistically small values [i.e., of order the capillary length (d_o)] takes two forms: spatial and temporal. The first, which deals with simultaneously resolving multiple spatial scales, can be largely eliminated through the use of multiscale algorithms such as adaptive-mesh refinement.[1,2] The second, less broadly appreciated, issue concerns the time scale (τ) in the phase-field equation, which characterizes the atomic attachment kinetics across the interface. For small W, corresponding values τ can be as small as 10^{-11} s, making it unfeasible to simulate microstructures on time scales relevant to materials science phenomena. Both these limitations have typically been overcome by artificially "accelerating" τ (and simultaneously enlarging W) to achieve results more rapidly. This, however, can give rise to spurious interface kinetics and solute trapping effects, particularly when modeling alloy solidification at experimentally relevant parameters.

In the last decade, significant progress has been made toward overcoming the thin-interface challenges inherent in phase-field modeling. The first step was taken by Karma and Rappel[3] for pure materials. By performing a matched asymptotic analysis to second order in the ratio of the phase-field interface width to the thermal diffusion length, an expression was obtained for the effective sharp-interface kinetic coefficient, which could be made to vanish in the limit $d_o \ll W \ll D/V$ (D and V are the diffusion coefficient and characteristic interface velocity, respectively). This seminal work opened a new window for reproducing the free-boundary kinetics of solidification using phase-field models employing large ratios of W/d_o. More importantly, it allowed a dramatic increase in the corresponding *time scale* governing phase-field simulations. In conjunction with advanced numerical algorithms, experimentally relevant simulations of dendritic growth were possible in hours rather than months.

For the case of binary alloy solidification of metal alloys, in which the solute diffusion coefficients in different phases can vary by several orders of magnitude, the situation is far more complex. A second order matched asymptotic analysis of various two-sided alloy phase-field models[2,4–6] reveals that their thin-interface limit gives rise to, in addition to the traditional sharp-interface boundary conditions, three "correction" terms that scale with the interface thickness. Two of these emerge precisely because of the two sidedness of diffusion. In the limit of rapid solidification, where the diffusion length of impurities becomes comparable to the interface width, these corrections reflect physically relevant additions to the usual sharp-interface models of solidification.[7–10] At low solidification rates, however, these corrections are not relevant, and their influence—inherent in all phase-field models—must be eliminated, particularly if diffuse interfaces are to be used for efficient computations.

For the specific case of a dilute, ideal, two-sided binary alloys, a method for eliminating the thin-interface corrections introduced by the diffuseness of the phase field was recently calculated by Karma and co-workers.[5,6] Their technique forgoes the thermodynamically consistent approach of deriving the phase and concentration equations from a common free energy functional. Instead, the mass conservation equation, once obtained through variation of the free energy, is modified as follows: (a) the interpolation function inherited by the chemical potential from the free energy is replaced by a separate interpolation function that can act as an independent degree of freedom; (b) the addition of a phe-

nomenological flux term (coined the "antitrapping" flux) is added to the mass conservation equation. This flux corrects for the solute trapping that occurs due to the inherent diffuseness of the phase-field interface. Conditions (a) and (b), and the freedom to choose the function that interpolates solute diffusion across the interface, provide three degrees of freedom with which to cancel the thin-interface correction terms discussed in the previous paragraph.

Another significant advantage afforded by the approach developed by Karma and co-workers is that it provides a methodology for choosing the entropy and internal energy interpolation functions in the free energy functional such that the steady state phase-field and concentration equations decouple for all values of the interface width (W). This allows the surface energy in the phase-field model to be set independently of concentration, a feature critical when making the phase-field interface diffuse for computational convenience. Otherwise, a concentration dependence to the surface energy would exist, detracting from the efficiency with which equivalent sharp-interface parameters can be calculated and subsequent computations carried out. It should be noted that there are alternative phase-field formulations that also decouple the phase and concentration equations.[11–13] However, a thin-interface (i.e., second order) asymptotic analysis for simulating these models in their corresponding sharp-interface limit is presently lacking.

The antitrapping technique has also been extended to the study of nonisothermal solidification of dilute ideal, binary alloys by Ramirez *et al.*[14] This situation exploits the fact that thermal diffusion relaxes on time scales several orders of magnitude faster than solute diffusion. This allows the temperature at the interface to be treated as quasistatically "frozen" in time relative to the dynamics of solute segregation. As a result, the dynamics of the solute diffusion can be evolved and/or corrected using the antitrapping flux technique developed in Refs. 5 and 6. Similar approaches can also be utilized to couple phase-field models of alloy solidification to other fast fields, such as electrostatic and elastic fields.[15]

More recently still, the antitrapping technique was also extended to the study of quantitative modeling of eutectic (i.e., two-phase) solidification by Folch and Plapp.[16] Their approach uses a phenomenological triple-well potential that approximates the free energy of each of three phases with an identical quadratic well. Following analogous approach to Ref. 6, the form of the free energy is chosen so as to decouple the steady state phase and concentration fields between any two coexisting phases. This fixes the *form* of the equilibrium chemical interpotential, whose parameters can then be fitted by the two sets of solidus and liquidus lines of any particular eutectic phase diagram. Following a suitable rescaling of their phase-field equations, their model can be approximately mapped onto that of Ref. 6 for any two coexisting phases. A limitation of the model of Ref. 16 is that it uses the metastable projections of the solidus lines to approximate the solid phase concentrations below the eutectic temperature.

To date, all quantitative phase-field models of solidification have been formulated for dilute ideal alloys, characterized by *linear* coexistence curves. An exception is the two-phase solidification model of Ref. 16, which can, in principle, be used to model solidification in alloys with nonlinear coexistence lines, but which has only thus far been applied to an alloy with linear solidus and liquidus coexistence lines. The formalism of Ref. 16 follows an analogous but independent approach to the one reported here.

This paper presents a phase-field formalism[15] that extends the antitrapping technique developed in Refs. 5 and 6 to the study of single-phase solidification in a binary alloy characterized by *nonlinear* solid-liquid phase coexistence boundaries. It is shown that Gibbs free energies of any two coexisting phases can be approximated by the functional form used for a dilute ideal alloy, modified, however, by *effective* (i.e., temperature-dependent) coefficients. This makes it possible to exploit the antitrapping machinery developed for dilute ideal alloys in Refs. 5 and 6 to reproduce the sharp-interface kinetics of single-phase solidification in binary alloys having arbitrary phase coexistence boundaries.

Section II presents the sharp-interface kinetics of solidification of a general binary alloy. Section III shows how Gibbs free energy of an arbitrary phase can be approximated, close to equilibrium, by the functional form of a dilute ideal free energy modified by effective, temperature-dependent parameters. Section IV shows how the parameters of the phase-field model of Refs. 5 and 6 can thus be made temperature dependent, making it possible to simulate the sharp-interface limit of solidification in a binary alloy with nonlinear phase coexistence curves. Section V presents simulations of isothermal and nonisothermal dendritic solidification in an isomorphous binary alloy. Solute partitioning and transient dendrite tip dynamics are shown to be convergent over a wide range of interface widths. Section VI compares the role of linear vs nonlinear phase coexistence lines on the growth rate of a solutal dendrites.

II. SHARP-INTERFACE KINETICS OF BINARY ALLOY SOLIDIFICATION

We begin by considering a sharp-interface model of single-phase solidification in a binary alloy made of components A and B, whose phase diagram has arbitrary solidus and liquidus lines. Starting with a liquid phase and cooling into the coexistence regions will initiate solidification of the solid phase. Assuming for the moment isothermal conditions, solidification is described by solute diffusion in each of the bulk phases and two corresponding boundary conditions at the solid-liquid interface: flux conservation and the Gibbs-Thomson condition. In the limit where the interface can be assumed to be mathematically sharp, these processes are expressed, respectively, as

$$\partial_t c = \nabla \cdot (M_{L,s} \nabla c), \tag{1}$$

$$(c_L - c_s) V_n = D_s \partial_n c|^+ - D_L \partial_n c|^-, \tag{2}$$

$$c_{L,s} - c_{L,s}^{\mathrm{eq}} = -\frac{2\sigma\Omega}{\Delta C_o \Lambda^{\pm}} \kappa, \tag{3}$$

where $c \equiv c(\vec{x},t)$ is the concentration field, $M_{s,L}(c) = \Omega D_{s,L} c(1-c)/RT$ is an expression for the mobility, with Ω

the molar volume of the phases, $D_{s,L}$ the solid and/or liquid diffusion coefficients, respectively, T the temperature, and R the natural gas constant. The notation $\partial_n c|^{\pm}$ represents the normal derivative on either side of the solid-liquid interface. In the last two equations, $c_{L,s}$ represents the concentrations on the liquid and/or solid side of the interface, σ is the surface energy of the solid and/or liquid interface, κ is the local interface curvature, and $\Delta C_o = c_L^{\mathrm{eq}} - c_s^{\mathrm{eq}}$, where $c_{L,s}^{\mathrm{eq}}$ represent the equilibrium liquid and/or solid concentrations at the given temperature. Finally, $\Lambda^{\pm} = \partial^2 G_{L,s}(c)/\partial c^2|_{c_{L,s}^{\mathrm{eq}}}$, where $G_{L,s}$ is the molar Gibbs free energy of the phase.

Following standard manipulations,[17] Eq. (3) can be expressed as

$$\frac{c_{L,s}}{c_{L,s}^{\mathrm{eq}}} = 1 - [1 - k(T)]\left[\frac{2\sigma T/L}{|m_{L,s}(T)|(1-k(T))c_L^{\mathrm{eq}}}\right]\kappa, \tag{4}$$

where

$$|m_{L,s}(T)| = \frac{RT^2[1-k(T)][\hat{G}''(c_{L,s}^{\mathrm{eq}})c_{L,s}^{\mathrm{eq}}]}{\Omega L} \tag{5}$$

and where we have defined

$$k(T) = \frac{c_s^{\mathrm{eq}}(T)}{c_L^{\mathrm{eq}}(T)} \tag{6}$$

as the temperature-dependent partition coefficient between solid and liquid phases, which is uniquely defined by the phase diagram of a particular alloy. Meanwhile, $\hat{G}''(c_{L,s}^{\mathrm{eq}})$ is the second derivative of the dimensionless molar Gibbs free energy evaluated at the equilibrium concentrations $c_{L,s}^{\mathrm{eq}}$ (made dimensionless by redefining $\hat{G} \equiv G/RT$). Finally, L is the latent heat of fusion.

From the point of view of the sharp-interface model, it can be assumed that $G''(c_s^{\mathrm{eq}})c_s^{\mathrm{eq}} \approx G''(c_L^{\mathrm{eq}})c_L^{\mathrm{eq}}$, which makes $m_s = m_L \equiv m(T)$, where $m(T)$ is the slope of the liquidus curve at temperature T. This approximation implies that the liquid phase capillary length d_o is used on both sides of the interface in the Gibbs-Thomson condition in Eq. (4). While this approximation becomes exact in dilute ideal alloys, it does not pose significant errors in the nondilute limit. Specifically, it only creates a small curvature-dependent error in the solid phase concentration, which is negligible at low solidification rates typical in metals.[16] In closing this section, it should be noted that Eq. (4) generates a curvature-induced correction in the interface concentration jump in Eq. (2) of the form $c_L - c_s = \Delta C_o\{1 - [1 - k(T)]d_o\kappa\}$.

III. APPROXIMATING THE GIBBS FREE ENERGY FUNCTIONAL

We next turn our attention to the construction of the Gibbs free energy function of a binary alloy phase labeled by the index ν. This will be used to motivate the choice of phenomenological phase-field free energy functional in the next section. Rather than attempting to approximate the Gibbs free energy of a phase over its entire concentration domain, we expand it, instead, to second order in a series around the equilibrium concentration $c = c_\nu^{\mathrm{eq}}(T)$. We will then require this expansion to be accurate only in the neighborhood of c_ν^{eq}. This approach is reasonable since at low undercooling, kinetics and curvature effects typically only cause the concentrations at the interface to deviate by a small amount from their equilibrium values.

Proceeding in this manner, we consider the following expansion for the Gibbs free energy of phase ν,

$$G_\nu = g_\nu(T) + a_\nu(T)(c - c_\nu^{\mathrm{eq}}) + b_\nu(T)(c - c_\nu^{\mathrm{eq}})^2 \cdots, \tag{7}$$

where

$$g_\nu(T) = f(T) - S_\nu(T)[T - T_m(T)] + \frac{RT}{\Omega}[\ln c_\nu^{\mathrm{eq}} + \epsilon_\nu'(T) - 1]c_\nu^{\mathrm{eq}}, \tag{8}$$

$$a_\nu(T) = \frac{RT}{\Omega}[\ln c_\nu^{\mathrm{eq}} + \epsilon_\nu'(T)], \tag{9}$$

$$b_\nu(T) = \frac{RT}{2\Omega c_\nu^{\mathrm{eq}}}. \tag{10}$$

The coefficient $S_\nu(T)$ is the entropy of the phase, while $\epsilon_\nu'(T) \equiv \epsilon_\nu(T)\Omega/RT$, where $\epsilon_\nu(T)$ is a free temperature-dependent parameter of the phase, which has units of energy density. The functions $f(T)$ and $T_m(T)$ are similarly functions of temperature that are to be determined.

The free parameters of G_ν are determined so that the free energy self-consistently reproduces certain relevant thermodynamic properties of a general binary alloy phase. We begin with the chemical interpotential defined by $\mu_\nu(T) = dG_\nu/dc|_{c_\nu^{\mathrm{eq}}}$. Equating $\mu_s = \mu_L$ gives

$$k(T) \equiv \frac{c_s^{\mathrm{eq}}}{c_L^{\mathrm{eq}}} = \exp\left(-\frac{(\epsilon_s - \epsilon_L)\Omega}{RT}\right), \tag{11}$$

which fixes the internal energy difference $\epsilon_s - \epsilon_L$ in terms of the partition coefficient at temperature T. Alternatively, $\epsilon_\nu(T)$ can be fixed in terms of the chemical potential and the equilibrium concentration of phase ν, $c_\nu^{\mathrm{eq}}(T)$, obtainable from thermodynamic databases and the phase diagram.

We next determine the function $f(T)$ by evaluating $G_\nu(c)$ a t c_ν^{eq}, giving

$$f(T) = S_\nu(T - T_m) + G_\nu(c_\nu^{\mathrm{eq}}) - \frac{RT}{\Omega}(\ln c_\nu^{\mathrm{eq}} + \epsilon_\nu' - 1)c_\nu^{\mathrm{eq}}. \tag{12}$$

Requiring that $f(T)$ be independent of phase ($\nu = s, L$) imposes the constraint

$$(T - T_m)(S_s - S_L) = \frac{RT}{\Omega}[1 - k(T)]c_L^{\mathrm{eq}}. \tag{13}$$

This allows us to self-consistently determine the reference parameter $T_m(T)$ in Eq. (8) by identifying $(S_s - S_L) = -L/T$, where L is the latent heat of fusion (we assume that L is independent of temperature, although making it depend on temperature would not change any of the arguments pre-

sented here). Equation (13) can thus be recast as an explicit condition on the parameter $T_m(T)$

$$T_m(T) = T + \left[\frac{RT^2[1-k(T)]}{\Omega L}\right] c_L^{\mathrm{eq}}(T). \tag{14}$$

The factor in the rectangular brackets of Eq. (14) is hereafter denoted by $m_d(T)$. Equation (14) defines a linear "phase diagram" that passes through the coordinates at $[T, c_L^{\mathrm{eq}}(T)]$ of the actual alloy phase diagram, and whose intercept $T_m(T)$ is temperature dependent.

It is noteworthy that the second derivative in Eq. (7), $c_L^{\mathrm{eq}} d^2 G_L / dc^2|_{c_L^{\mathrm{eq}}}$, is equal to that of a dilute ideal binary alloy phase. It may thus appear that a phase-field free energy based on Eq. (7) will only allow us to model a capillary length d_o of dilute ideal binary alloys [via Eqs (4) and (5)]. While this approximation becomes exact for dilute alloys, it will not limit our phase-field simulations at nondilute concentrations. Specifically, it will be shown in the next section that the freedom to self-consistently alter the interface width and coupling constant in the phase-field model can actually be used to map the phase-field capillary length onto *any* value.

It is convenient to cast the free energy expansion in Eq. (7) in terms of a more tractable analytical form, which will later allow us to link our phase-field free energy functional to that used in Refs. 5 and 6. To do so, we note that the form of $G_\nu(c)$ defined by Eq. (7) is precisely a second order Taylor series expansion of the function

$$G_\nu(c) = f(T) - S_\nu(T - T_m(T)) + \frac{RT}{\Omega}(c \ln c - c) + \epsilon_\nu c, \tag{15}$$

about $c = c_\nu^{\mathrm{eq}}$, where all parameters in Eq. (15) have the temperature dependence defined above. It should be emphasized that while Eq. (15) has the same *analytical form* used to model ideal solutions, its parameters are quite different. Indeed, as shown above, through the effective temperature dependence of the parameters in Eq. (15), we can approximate to a reasonable accuracy several relevant properties of a *general* binary alloy phase near $c = c_\nu^{\mathrm{eq}}$.

IV. PHASE-FIELD MODEL FOR SOLIDIFICATION OF BINARY ALLOYS

The starting point of our phase-field formulation is the free energy functional given by

$$G = f(T) - S(\phi)(T - T_m) + \frac{RT}{\Omega}(c \ln c - c) + \epsilon(\phi)c, \tag{16}$$

where ϕ is the usual order parameter that continuously interpolates between solid ($\phi = 1$) and liquid ($\phi = -1$). The functions for the entropy $S(\phi)$ and internal energy $\epsilon(\phi)$ interpolate between their respective values in each phase [i.e., $S(\phi = \pm 1) \to S_{s,L}$ and $\epsilon(\phi = \pm 1) \to \epsilon_{s,L}$]. The temperature dependent and bulk parameters in each phase ν are as defined in the previous section. The form of interpolation functions is chosen precisely as in Refs. 5 and 6 in order to guarantee that the concentration and phase-field equations introduced below decouple at steady state, even for large values of the interface width (W).

Substituting the free energy functional in Eq. (16) into the standard dynamical equations of motion for the phase and solute fields;[2,5,6] considering, for the moment, a constant temperature T and following the procedure of Ref. 6, the following dimensional phase-field equations of solidification can thus be obtained:

$$\begin{aligned}
\tau(T)A(\hat{n})^2\frac{\partial\phi}{\partial t} &= \hat{\nabla}\cdot[W(T)^2A(\hat{n})^2\hat{\nabla}\phi] \\
&\quad + \phi - \phi^3 - \lambda(T)(1-\phi^2)^2U \\
&\quad + \hat{\nabla}\cdot\left(|\hat{\nabla}\phi|^2W(T)^2A(\hat{n})\frac{\partial A(\hat{n})}{\partial(\hat{\nabla}\phi)}\right), \\
\left(\frac{1+k(T)}{2} - \frac{1-k(T)}{2}\phi\right)\frac{\partial U}{\partial t} &= \hat{\nabla}\cdot\left(D(T)\frac{1-\phi}{2}\hat{\nabla}U + \frac{1}{2\sqrt{2}}\{1+[1-k(T)]U\}\frac{\partial\phi}{\partial t}\frac{\hat{\nabla}\phi}{|\hat{\nabla}\phi|}\right) \\
&\quad + \frac{1}{2}\{1+[1-k(T)]U\}\frac{\partial\phi}{\partial t},
\end{aligned} \tag{17}$$

where $D(T)$ is the liquid state diffusivity, $U = (e^u - 1)/[1 - k(T)]$, and

$$u = \ln\left\{\frac{(2c/c_L^{\mathrm{eq}})}{1 + k(T) - [1 - k(T)\phi]}\right\}. \tag{18}$$

The function $A(\hat{n})$ is a fourfold anisotropy coefficient,[1,3,5,6] where $\hat{n}$ is the normal vector at the interface. The parameter $W(T)$ is the interface width and $\tau(T)$ interface kinetic attachment time, both of which may be temperature dependent as shown below. The parameter $\lambda(T)$ is the coupling coefficient, formally dependent on the nucleation barrier height and temperature. In thin-interface phase-field modeling, $\lambda(T)$ is treated as a convergence parameter. Finally, we note that by using the same antitrapping term defined in Refs. 5 and 6 in the U equation, we can eliminate *all* thin-interface correction terms appearing in the thin-interface limit of Eq. (17).

The model equations (17) are identical in form to that examined in Ref. 6. This connection allows us to employ the same parametric relationships between $\lambda(T)$, $W(T)$, and $\tau(T)$ defined in Ref. 6 to map Eq. (17) onto the sharp-interface model in Eqs. (1), (2), and (4). Specifically, the solutal capillary length can be related to the phase-field model parameters as

$$a_1\frac{W(T)}{\lambda(T)} = d_o(T) \equiv \frac{\Gamma}{\Delta T}, \tag{19}$$

where $a_1 = 0.8839$,[5] $\Gamma = \sigma T/L$, $\Delta T = |m(T)|[1-k(T)]c_L^{\mathrm{eq}}(T)$, and $m(T) = m_L(T)$ as defined by Eq. (5). We note that $\lambda(T)$ can be treated as an adjustable convergence parameter in phase-field simulations of Eq. (17).[5,6] As such, we can model *any* capillary length $d_o(T)$ via Eq. (19) by suitably adjusting $W(T)$.

We can also identically set the interface kinetic coefficient to zero in our phase-field simulations [to second order accuracy in the ratio W/d_o (Refs. 2, 5, and 6)] by setting interface kinetic time scale to

$$\tau(T) = \frac{a_2 \lambda(T)}{D} W^2(T), \tag{20}$$

where $a_2 = 0.6267$.[5] As mentioned above, the coupling constant $\lambda(T)$ may be chosen arbitrarily since its value does not affect the convergence of the dendritic tip velocity and radius, provided it is small enough.[3,5,6] From Eq. (21), the dimensionless diffusion constant can be seen equal to $a_2\lambda(T)$ when the phase field equations are nondimensionalized using $\tau(T)$ as the time scale and $W(T)$ as the length scale.

Our approach can also incorporate nonisothermal conditions. Specifically, in the limit when the thermal diffusion coefficient is much larger than the solute diffusion coefficient in the liquid (typically $D_L/\alpha \sim 10^{-4}$), it is reasonable to model temperature as an imposed field that adjusts quasi-instantaneously to changes in the concentration and phase (i.e., $\partial T/\partial t \approx 0$). In this work, we study the case $T \rightarrow T(t)$ in Eq. (17), which makes $k(T)$ and $d_o(T)$ time dependent. This in turn makes $W(T)$ and $\tau(T)$ time dependent due to Eqs. (19) and (20). The coupling parameter $\lambda(T)$ can again be set to a constant.

We found that it is more convenient to maintain the interface width W fixed as temperature changes, thus shifting the temperature dependence in Eqs. (19) and (20) onto $\lambda(T)$. In particular, comparing Eq. (19) at two different temperatures with the requirement that W stay fixed requires that λ change with temperature according to

$$\lambda(T) = \frac{[1-k(T)]}{[1-k(T_0)]} \frac{c_L^{\mathrm{eq}}(T)}{c_L^{\mathrm{eq}}(T_0)} \frac{m(T)}{m(T_0)} \lambda(T_0), \tag{21}$$

where the subscript 0 refers to the initial temperature at $t=0$ (e.g., the first temperature of entry into the coexistence region) and where $T \equiv T(t)$ is the temperature at time t. With the record of $\lambda[T(t)]$, and fixed W, Eq. (20) can be used to calculate the kinetic time scale $\tau[T(t)]$.

V. SIMULATIONS AND CONVERGENCE TESTS FOR ISOTHERMAL AND NONISOTHERMAL SOLIDIFICATION IN AN ISOMORPHOUS ALLOY

To demonstrate the feasibility of our approach, we considered dendritic solidification of an A-B binary alloy with an isomorphous phase diagram, two examples of which are shown in Fig. 1. This phase diagram is obtained by applying a common tangent construction to the solid and/or liquid alloy free energy defined in Ref. 7. The liquidus and solidus concentrations are given by

$$c_s^{\mathrm{eq}}(T) = \frac{1 - e^{-2\Delta T^A/RT}}{e^{-2\Delta T^B/RT} - e^{-2\Delta T^A/RT}},$$

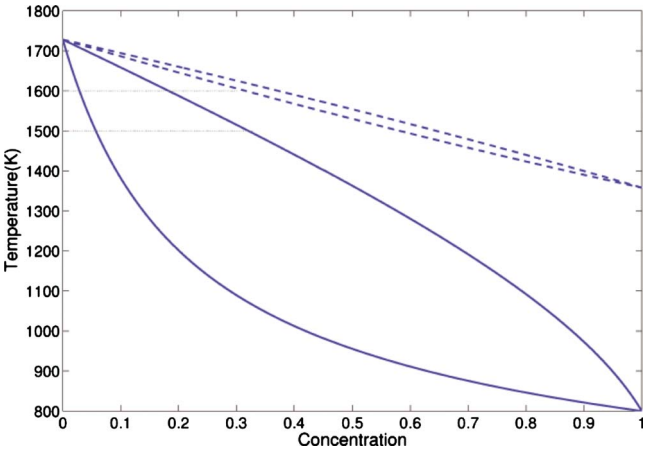

FIG. 1. (Color online) Phase diagrams for Ni-Cu binary alloy (broken lines) and the A-B alloy studied in this work (solid lines).

$$c_L^{\mathrm{eq}}(T) = \frac{1 - e^{-2\Delta T^A/RT}}{1 - e^{(-2\Delta T^A + 2\Delta T^B)/RT}}, \tag{22}$$

where $\Delta T^i = L^i(T_m^i - T)/2T_m^i$ with $i = A, B$ and T_m^i is the melting temperature of component i, while L_i is its latent heat. The material properties of the A-B alloy used in this work are $L^A = 31\,000$ J/mol, $L^B = 24\,622$ J/mol, $c_p^A = 26.07$ J/mol, $c_p^B = 24.02$ J/mol, $T_m^A = 1728$ K, $T_m^B = 800$ K. This corresponds to the phase diagram with the solid lines in Fig. 1. As a comparison, the material properties of a Ni-Cu binary alloy are the same as those of our hypothetical A-B binary alloy except that the latent heats of Ni and Cu are half of those of A, B, respectively, and the melting point of Cu is 1358 K.

From the liquid-solid coexistence concentrations in Eq. (22), the partition coefficient is given by $k(T) = c_s^{\mathrm{eq}}(T)/c_L^{\mathrm{eq}}(T)$. Meanwhile, $1/m(T) \equiv dc_L^{\mathrm{eq}}(T)/dT$. We note that the choice of the isomorphous alloy defined by Eq. (22) is one example of a physically motivated alloy system on which to demonstrate our approach. This approach has also been recently used to study isothermal phase transformations in other alloys[15] and will be reported in a future publication.

The phase-field equations (17) were used to simulate both isothermal quenches (fixed $T = T_0$) and nonisothermal cooling [initial temperature $T = T_0$ to temperature $T(t)$] through the coexistence region of Fig. 1. The phase-field equations were made dimensionless by rescaling length by the initial interface width $W(T_0)$ and time by the initial kinetic time $\tau(T_0)$, both of which were determined after an initial $\lambda(T_o)$ was chosen. For nonisothermal conditions, the coupling constant was determined dynamically using Eq. (21). Equations (6) and (22) were used to calculate $k(T)$ and $m(T)$. The time scale was tracked though $\tau(T) = [d_0(T)^2/D]a_2\lambda^3(T)/a_1^2$, which implies that Eq. (20) was applied to simulate vanishing interface kinetics.[5,6] The initial value of $\lambda(T_0)$ was chosen arbitrarily. We note that since $d_0(T) \sim 1/\Delta T$ and $W(T) = \lambda(T)d_0(T)/a_1$, the interface width $W(T)$ remains unchanged from its initial value $W(T_0)$ when Eq. (21) is applied. The time scale, however, is changed by a factor $\tau(T)/\tau(T_0) = \Delta T/\Delta T_0$. Finally, we have neglected, without loss of gen-

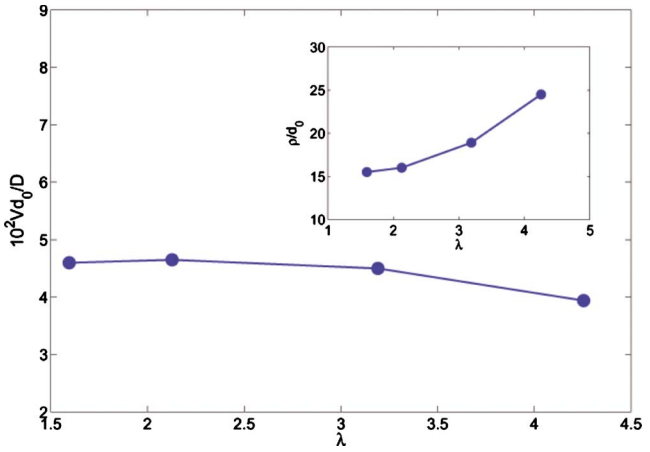

FIG. 2. (Color online) Predicted dimensionless steady-state tip velocities as a function of $\lambda(T_0)$ for isothermal solidification of the *A-B* binary alloy in Fig. 1, with quench temperature $T_0=1450$ K and initial concentration corresponding to the liquidus concentration at temperature 1600 K. Tip velocities were evaluated after steady state had been established. The inset shows the steady-state tip radius as a function of $\lambda(T_0)$. Simulations were conducted in the same physical domain and started from the same initial seed size and initial conditions (see text).

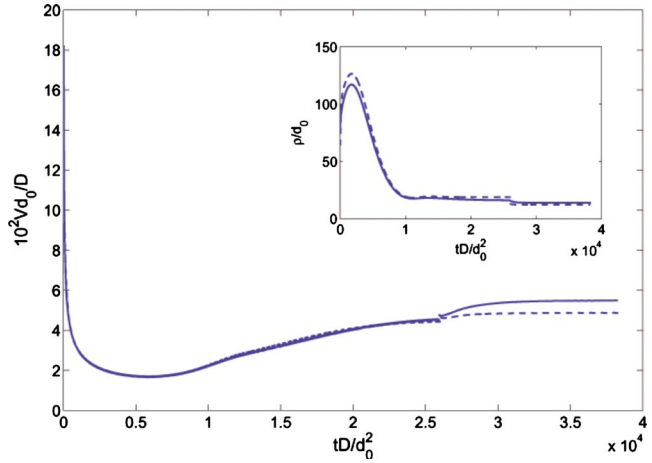

FIG. 3. (Color online) Comparison of temporal evolution of dimensionless tip velocity for nonisothermal solidification conditions corresponding to an initial quench to $T_0=1450$ K and subsequently to 1400 K. The two cases shown correspond to $\lambda(T_0)=2.1275$ (solid line) and 3.1913 (broken line). The change in temperatures occurs at the jump in the curves. The inset compares the temporal evolution of the corresponding dimensionless tip radius. Other parameters are described in the text.

erality, the temperature dependence of σ [Eq. (4)].

As a consistency check, we first performed isothermal two dimensional dendritic growth simulations to investigate the convergence behavior of the tip radius and tip velocity for decreasing values of the coupling constant $\lambda(T_0)$. Four different values of $\lambda(T_0)$ (and hence, interface width) were examined: $\lambda(T_0)=1.5957, 2.1275, 3.1913, 4.2550$. Simulations were performed on a uniform mesh with a numerical grid size set to $\Delta x=0.4W(T_0)$ and the physical domain was chosen to be the same for all $\lambda(T_0)$, i.e., $800\times800W$, $600\times600W$, $400\times400W$, and $300\times300W$, respectively. Explicit time marching was used to solve the phase-field equations, with a time step of $\Delta t=0.02$, 0.02, 0.018, and 0.014 [in units of $\tau(T_0)$] for the four $\lambda(T_0)$, respectively. The choice of physical domain size $(1444d_o)$ was chosen so that simulations were free of finite-size effects. All simulations started from the same physical seed size. The form of the initial concentration and phase fields was chosen as in Ref. 5.

In our isothermal simulations, the far-field (i.e., average) concentration was chosen to be $C_L(\infty)=0.1827$, corresponding to the liquidus concentration at 1600 K. The solidification quench temperature was set to $T_o=1450$ K, corresponding to an equilibrium liquidus concentration of $C_L^{\mathrm{eq}}=0.3875$ and a partition coefficient $k=0.1902$. Figure 2 shows the dimensionless steady state tip velocity and tip radius for the different $\lambda(T_0)$ discussed in the previous paragraph. The tip velocity converges faster than tip radius with decreasing $\lambda(T_0)$; however, both are very nearly converged for $\lambda(T_0)\approx2.1275$. The corresponding centerline solute concentration was also found to agree well with the Gibbs-Thomson relation $c_s/c_l^{\mathrm{eq}}=k[1-(1-k)d_0\kappa]$ for all $\lambda(T_0)$.

We next considered a simple case of nonisothermal solidification of our *A-B* alloy to investigate convergence of our method for transient situations. An *A-B* alloy with a far-field concentration corresponding to the liquidus concentration at 1600 K was first quenched to $T_0=1450$ K and solidified isothermally until nearly reaching steady state, after which the alloy was quenched to $T=1400$ K and a new dendrite steady state was reached. The temporal evolution of dimensionless tip velocity and tip radius for the choices of $\lambda(T_0)=2.1275$ and 3.1913 are shown in Fig. 3. Numerical grid size, system sizes, time steps and initial conditions were the same as those of the corresponding $\lambda(T_0)$ used in Fig. 2. The change in dimensionless steady state tip velocity and radius after the quench temperature is changed does show some dependence on the choice of $\lambda(T_0)$. This is consistent with the isothermal convergence test shown in Fig. 2. Namely, after quenching to 1400 K, the temperature-dependent coupling constant becomes $\lambda(T)=1.1803\lambda(T_0)$; therefore, effectively, we are comparing the convergence at two larger coupling constants, which is prone to more error. However, these changes are within 10% of each other, which is in reasonable agreement.

Figure 4 plots the solute distribution along the dendrite centerline for the case corresponding to $\lambda(T_0)=3.1913$ in Fig. 3. The figure shows the concentration profile with and without the use of antitrapping in the phase-field equations. We found that solute partitioning in the solid obeys the Gibbs-Thomson relation quite well when the antitrapping is turned on, while the concentration in the solid phase displays significant error when antitrapping is switched off. This demonstrates the capability of the antitrapping flux in the concentration equation to cancel solute trapping due to the diffuse interface between solid and liquid phases.[5]

A second nonisothermal situation examined continuous cooling between two temperatures during solidification. An *A-B* alloy with the same initial concentration as in the previous nonisothermal test was first cooled to 1450 K and iso-

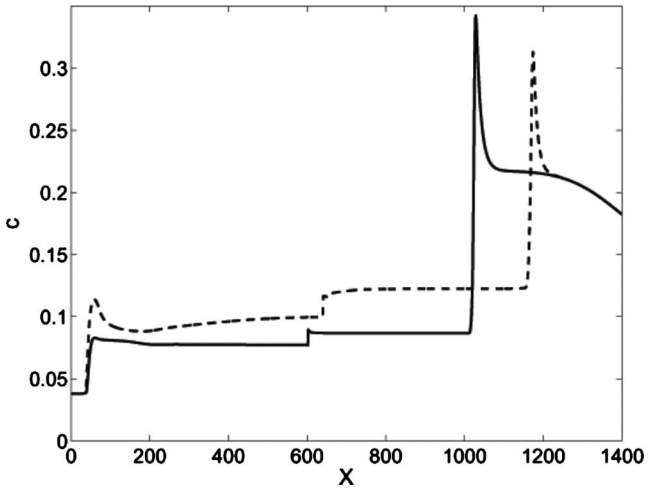

FIG. 4. Plots of solute concentration (in molar fraction) along the centerline dendrite axis for the nonisothermal case corresponding to $\lambda(T_0)=3.1913$ in Fig. 3. The solid line corresponds to the case when antitrapping is turned on, while the broken line corresponds to the case that antitrapping is switched off. The x axis is in units of Δx corresponding to the $\lambda(T_0)=3.1913$ case of Fig. 2.

thermal solidification again proceeded until the dendrite tip velocity nearly reached steady state (~26 000 dimensionless time steps as shown in Fig. 5). Then the alloy was stepwise cooled one degree per step at equal time intervals down to 1400 K, following which isothermal solidification continued at 1400 K from about 40 000 dimensionless time steps. Figure 5 shows the dimensionless dendrite tip speed and radius corresponding to $\lambda(T_0)=2.1360$, 2.4061, and 3.1913. Numerical grid size, system sizes, and initial conditions were chosen as in Fig. 2. Time steps were $\Delta T=0.02, 0.018, 0.018$ for the three $\lambda(T_0)$, respectively. The data indicate good convergence of our method in the transient and steady state regimes. As a comparison Fig. 5 also shows the tip velocity and radius vs time for the case of $\lambda(T_0)=2.1360$ with no antitrapping current used in the phase-field equations (18). Without antitrapping, there is a systematic shift in the radius at all times and in the velocity over most of the time domain.

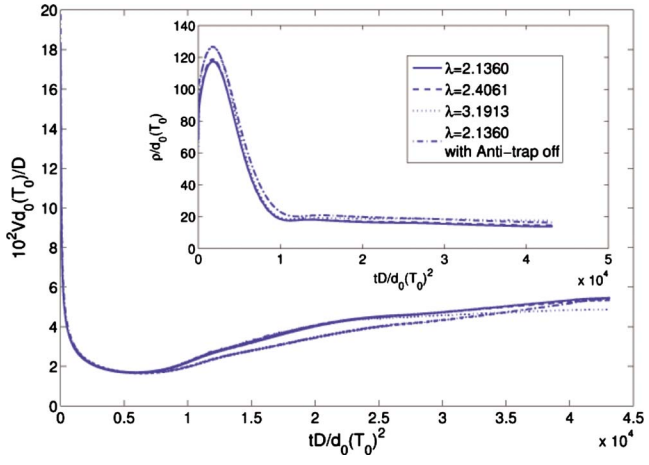

FIG. 5. (Color online) Temporal evolution of dimensionless tip velocity for nonisothermal solidification conditions corresponding to slowly cooling from 1450 to 1400 K. Three values of $\lambda(T_0)$ are compared. The inset compares the temporal evolution of the dimensionless tip radius for the same simulation parameters. Also displayed are the results for a case without antitrapping in the phase-field equations. Other parameters are described in the text.

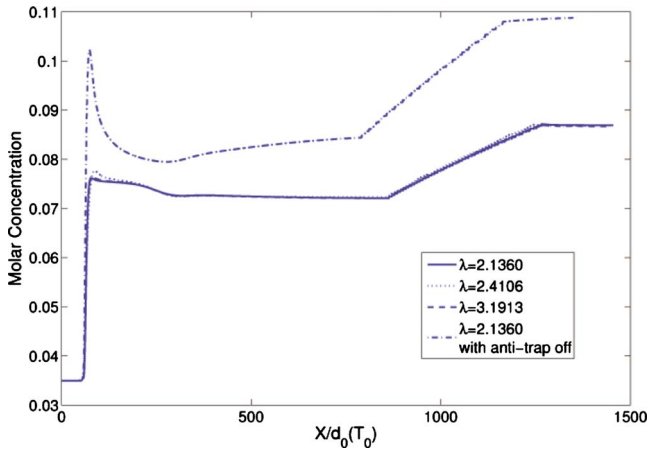

FIG. 6. (Color online) Plots of dendrite centerline solute concentration (in molar fraction) corresponding to the three $\lambda(T_0)$ values simulated in the data of Fig. 5. For comparison, a case without antitrapping is also shown.

Figure 6 plots the centerline concentration along the dendrite axes for the three values of $\lambda(T_0)$ simulated in the transient data of Fig. 5. The convergence of concentration for the different $\lambda(T_0)$ is excellent in both the transient and steady state regimes. As a comparison, the centerline concentration for the case of $\lambda(T_0)=2.1360$ *without* antitrapping is also plotted, showing a very large deviation from the case with antitrapping, the latter of which was again found to obey the Gibbs-Thomson boundary condition.

VI. EFFECT OF LINEAR VERSUS NONLINEAR PHASE BOUNDARIES ON DENDRITE TIP SPEED

This section compares the effect of linear vs nonlinear phase boundaries on dendrite tip velocity. In the dilute limit of an isomorphous alloy, the liquidus and sodidus lines are linear, thus in order to see a difference between linear vs nonlinear phase boundaries, we performed simulations in the nondilute region of the isomorphous phase diagram. The parameters of the *A*-*B* isomorphous phase diagram are as specified in the previous section. The parameters of the corresponding linear phase diagrams are indicated below. Simulation in this section were done with $\lambda(T_0)=3.1913$. Numerical grid spacing, domain size, and initial conditions for these simulations were the same as those of the corresponding $\lambda(T_0)$ in Fig. 2. The simulation time step was set to $\Delta t=0.01$.

The first case considered was continuous cooling through the isomorphous phase diagram from 1500 to 1400 K with far-field alloy concentration corresponding to a liquidus temperature of 1600 K. The corresponding linear phase boundaries against which the comparison was made were con-

structed by connecting the two respective points on the liquidus and solidus lines at 1400 K with the melting point T_m^A. This gave the same final supersaturation, $\{\Omega=[c_l^0(T)-c_\infty]/[c_l^0(T)-c_s^0(T)]\}$ for both alloy systems at the final quench temperature (i.e., 1400 K). In both cases, the same $\lambda(T_0)=3.1913$ was used. The dimensionless tip velocities for these two phase diagrams only differed by approximately 5%. This small difference arises because for temperatures in region from the melting point T_m^A down to 1400 K, the liquidus and solidus lines of the isomorphous phase diagram essentially follow those of the linear phase diagram.

We next considered cooling into the temperature region of the isomorphous phase diagram exhibiting a more pronounced nonlinearity in the shape of the liquidus and solidus lines. We chose an alloy with a far-field concentration $C_L(\infty)=0.5768$ corresponding to a liquidus temperature of 1300 K. The alloy was quenched to $T_0=1200$ K and then stepwise cooled one degree per time step down to 1000 K. At 1000 K, the final supersaturation was $\Omega=0.6578$, and the solute partition coefficient was $k=0.4770$. As described in the previous paragraph, the corresponding linear phase boundaries of the comparative ideal dilute model were chosen to intersect the liquidus and solidus of the isomorphous phase diagram at the temperature of 1000 K, and to converge at the melting point T_m^A. In both cases, simulations were conducted with $\lambda(T_0)=3.1913$. The dendrite tip speeds for the two cases are shown in Fig. 7. For this case, the linear vs nonlinear phase boundaries gave rise to a significant difference in the transient and steady state dendrite tip speed. We also examined the temporal evolution of dendrite tip radii for these two cases. Interestingly, we found that there was only about a 5% difference in tip radii for the two cases.

The data of Fig. 7 show that despite cooling both alloys to the same final supersaturation, the transient and steady state tip speeds can be significantly affected by the path the interface concentrations traverse through their corresponding phase diagrams during cooling. We expect these results to be important in quantitative modeling of transient dendritic growth dynamics and phase compositions, the latter of which is particularly important in modeling realistic casting situations.

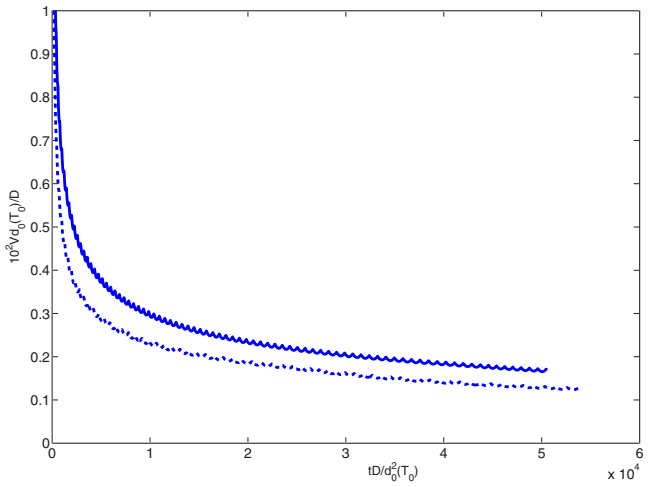

FIG. 7. (Color online) Comparison of the temporal evolution of dimensionless tip velocity for linear vs nonlinear phase boundaries. The broken lines correspond to linear phase boundaries. The simulation parameters are $\lambda(T_0)=3.1913$, $\Delta x=0.4W(T_0)$, the system size is $400\times400W(T_0)$ and $\Delta t=0.01$.

VII. SUMMARY

A formalism for performing quantitative phase-field simulations of single-phase solidification in binary alloys with *nonlinear* coexistence phase boundaries was presented. It was shown that, close to equilibrium, the Gibbs free energy of two coexisting phases can be approximated analytically by the free energy form of dilute, ideal binary solution with effective temperature-dependent coefficients. This result enables us to exploit the thin-interface asymptotic analysis developed previously for a phase-field model of a dilute ideal binary alloys exhibiting linear solidus and liquidus lines.

Isothermal and nonisothermal dendritic solidification was simulated in an *A-B* alloy with an isomorphous phase diagram. Dendrite growth rates and solute segregation were measured and found to be convergent for different interface thicknesses. Simulations of dendritic growth in alloys with linear versus nonlinear phase boundaries demonstrated that the morphology of the liquidus and solidus phase boundaries can significantly influence phase compositions and dendritic growth rates during solidification. Finally, it is expected that one can also proceed along the lines presented here to develop antitrapping models for multicomponent alloys.

ACKNOWLEDGMENT

We would like to thank the National Science and Engineering Research Council of Canada (NSERC) and the Canadian Space Agency for financial support of this work.

*provata@mcmaster.ca

[1] N. Provatas, N. Goldenfeld, and J. Dantzig, Phys. Rev. Lett. **80**, 3308 (1998).
[2] N. Provatas, M. Greenwood, B. Athreya, N. Goldenfeld, and J. Dantzig, Int. J. Mod. Phys. B **19**, 4525 (2005).
[3] A. Karma and W.-J. Rappel, Phys. Rev. E **53**, R3017 (1996).
[4] R. Almgren, SIAM J. Appl. Math. **59**, 2086 (1999).
[5] A. Karma, Phys. Rev. Lett. **87**, 115701 (2001).
[6] B. Echebarria, R. Folch, A. Karma, and M. Plapp, Phys. Rev. E **70**, 061604 (2004).
[7] N. A. Ahmad, A. A. Wheeler, W. J. Boettinger, and G. B. McFadden, Phys. Rev. E **58**, 3436 (1998).
[8] W. J. Boettinger and J. A. Warren, J. Cryst. Growth **200**, 583 (1999).

[9] D. Danilov and B. Nestler, Phys. Rev. Lett. **93**, 215501 (2004).
[10] J. Fan, M. Greenwood, M. Haataja, and N. Provatas, Phys. Rev. E **74**, 031602 (2006).
[11] H. Garcke, B. Nestler, and B. Stoth, SIAM J. Appl. Math. **60**, 295 (1999).
[12] I. Steinbach and F. Pezzolla, Physica D **134**, 385 (1999).
[13] S. G. Kim, W. T. Kim, T. Suzuki, and M. Ode, J. Cryst. Growth **261**, 135 (2004).
[14] J. C. Ramirez, C. Beckermann, A. Karma, and H. J. Diepers, Phys. Rev. E **69**, 051607 (2004).
[15] M. Greenwood, Ph.D. thesis, McMaster University, 2005.
[16] R. Folch and M. Plapp, Phys. Rev. E **72**, 011602 (2005).
[17] H. Reiss, *Methods of Thermodynamics* (Dover, New York, 1996).